3 Detailed thermophysical modeling

A detailed thermophysical model (TPM) is presented which is applicable to all asteroids including NEAs. The effects of thermal inertia, spin state, irregular shape, and thermal-infrared beaming are explicitly taken into account. Arbitrary convex shapes are allowed for, a generalization to non-convex shapes is under development (see chapter A in the appendix).

Realistic thermophysical modeling is required in order to reach the primary goal of this thesis, namely to determine the thermal inertia of NEAs through analysis of thermal-infrared observations; we wish to emphasize that there is no other well-established method of measuring the thermal inertia of asteroids. Furthermore, since the thermal physics of asteroid surfaces is here modeled in a more realistic way than in the highly idealized thermal models described in the previous chapter, TPM-derived estimates on diameter and albedo are potentially more accurate.

The thermal emission of NEAs is more challenging to model than that of MBAs due to their larger thermal inertia and because they are typically observed at much larger solar phase angles. While TPMs applicable to MBA data have previously been available, we here report the first TPM shown to be applicable to NEA data.

After an overview section, the thermal physics of asteroid surfaces is discussed in sect. 3.2. The model implementation is presented in sect. 3.3, validation test are presented in sect. 3.4. Sect. 3.5 is devoted to fitting techniques.

3.1 Overview

Various models have been proposed to overcome the limitations of simple thermal models. E.g., Hansen (1977) proposed a physical model for asteroid surface roughness along with an approximative treatment of conduction on a spherical asteroid. Non-spherical asteroid shapes have been modeled by Brown (1985), who proposed a variant of the STM with ellipsoidal asteroid shape. Spencer (1990) proposed an improved variant of Hansen's model in which thermal conduction is modeled in more detail. A variant of Spencer's model has been used by Delbo' (2004). The

most realistic asteroid TPM currently available is that by Lagerros (1996, 1997, 1998a) in which thermal conduction and surface roughness are explicitly modeled on an asteroid of arbitrary shape. The Lagerros TPM has been widely used and is well tested for applications to large MBAs. It enabled their thermal emission to be studied to such a high accuracy that they are used as calibration standards for space telescopes (see, e.g., Müller and Lagerros, 1998, 2002).

TPMs for asteroids were largely inspired by observations and models of other atmosphereless bodies. The first extraterrestrial body with well understood thermal properties was the *Moon*. It was found to display a thermal-infrared beaming effect by Pettit and Nicholson (1930) who also concluded that the thermal conductivity of lunar regolith was extremely low (see also Wesselink, 1948). Around the Apollo era the thermal properties of the Moon were studied in great detail from ground-based observations, in-situ measurements, and laboratory analysis of returned lunar samples (see, e.g., Buhl et al., 1968; Winter and Krupp, 1971; Saari and Shorthill, 1972; Jones et al., 1975; Langseth et al., 1976, and references therein). While Martian results are not directly applicable to asteroids due to Mars' atmosphere, lessons can be learned from spacecraft observations of *Martian satellites* (see, e.g., Lunine et al., 1982; Kührt et al., 1992), which are thought to be captured asteroids. Also *Mercury* is an atmosphereless body with a well observable and well modeled beaming effect (Emery et al., 1998). Due primarily to its slow spin, only the vicinity of Mercury's terminator is expected to be influenced appreciably by thermal inertia. No effects of thermal conduction on Mercury could be found from ground-based observations, but thermal-infrared spacecraft observations using the MERTIS instrument (Benkhoff et al., 2006) on BepiColombo are to be expected in the future.

Our TPM is based on that by Lagerros (1996, 1997, 1998a). Minor improvements to the physical modeling are proposed. The implementation is completely independent of Lagerros'. The model code was verified to produce physical results for very large solar phase angles and for a thermal inertia up to that of bare rock; extensive tests are reported in sect. 3.4. No such tests of the Lagerros TPM have been reported, but it is clear that his model was primarily aimed at application to MBAs. For geometric reasons, ground-based observations of MBAs cannot be performed at phase angles largely exceeding 30°. Furthermore, the typical thermal inertia of MBAs appears to be comparable to that of lunar regolith. For both reasons, modeling the thermal emission of MBAs is numerically less challenging than that of NEAs.

Our model is implemented in an object-oriented way (in C++) which makes it easy to add new features.

3.1.1 Model description

The asteroid is modeled as a convex mesh of typically a few thousand triangular facets. It is assumed to rotate about a fixed axis, i.e. non-principal-axis rotation ("tumbling") is not supported. All physical surface properties, such as albedo, emissivity, thermal inertia, and surface roughness are assumed to be constant over the surface. Local surface temperatures are calculated from the local insolation geometry. One-dimensional thermal conduction into and from the subsoil is taken into account, all relevant parameters are assumed to be constant. To model surface roughness, model craters in the form of subdued hemispheres are added. The crater density and opening angle can be varied. Inside craters, shadowing, multiple scattering of optical and thermal flux, and reabsorption of both are fully taken into account, leading to thermal-infrared beaming.

Global-scale convexity The asteroid shape model is assumed to be convex, only small-scale concavity is modeled in terms of craters. Global-scale convexity implies that facets cannot shadow one another, neither can they exchange energy radiatively which would lead to mutual heating. Since facets are typically very large compared to the penetration depth of the diurnal heat wave (see sect. 3.2.2), lateral heat conduction between facets can be neglected. Hence, the thermal flux emanating from an individual facet can be calculated independent of all other facets, which significantly simplifies the numerical treatment. A more general model variant, in which non-convex shape is allowed for, is described in chapter A in the appendix.

Most available models of asteroid shapes are convex by design (see Kaasalainen et al., 2002, for a review). Lacking such a shape model, one typically assumes a spherical or ellipsoidal shape, which are also convex.

3.1.2 Model parameters

Required asteroid parameters are the shape and spin state (see sect. 3.2.1 for details), the absolute optical magnitude H, slope parameter G, and emissivity ϵ. Model variables are the geometric albedo p_{V} (which determines the diameter D through H, and furthermore the Bond albedo A), the thermal inertia in SI units

(J $s^{-1/2}K^{-1}m^{-2}$), and the crater density and opening angle (in degrees). Model fluxes are calculated for a given Julian date, wavelength (in µm), and observing geometry, where the latter is defined by the heliocentric and observer-centric asteroid position in ecliptic coordinates (ecliptic longitude and latitude in degrees, distance in AU). Data taken at different epochs should be stored in separate fit files, but they can be read in and fitted simultaneously. Our techniques to fit model parameters to a given set of data are described in sect. 3.5.

3.1.3 Implementation overview

The TPM program takes `.convex` files as input. Those are generated using auxiliary programs based on computer-readable shape models (see sect. 3.2.1). On each facet, the diurnal temperature distribution is calculated as described in sect. 3.2.2. Thermal-infrared beaming is modeled as described in sect. 3.2.3. Disk-integrated model fluxes are calculated by summing up contributions from all visible facets.

3.2 Thermal physics

3.2.1 Global shape and spin state

In our TPM, the asteroid shape is modeled as a mesh of typically a few thousand planar triangular facets, the typical format of available asteroid shape models. The shape is defined by the coordinates of n vertices which form $2n - 4$ facets, each defined by the three indices of its vertices. As is common practice, a body-centric coordinate system is used in which the z axis corresponds to the spin axis; non-principal-axis rotation ("tumbling") is not supported so far. To model spherical and ellipsoidal shapes, an auxiliary program was developed which produces models of triangulated spheres of user-specified resolution and stretches them into ellipsoids if desired.

Geometric and thermal model tasks are separated in the code as far as possible, such that time-consuming geometric calculations need to be performed only once per shape. To this end, auxiliary programs have been developed to convert shape model files provided by colleagues (currently, the quasi-standard OBJ wavefront format and Mikko Kaasalainen's variant thereof are supported) into a specifically defined type called `.convex`. For the thermal emission of convex asteroids the vertex positions are irrelevant, hence `.convex` files contain solely a list of $2n - 4$ outbound surface-normal vectors (see sect. 3.2.1.a) and the model's intrinsic

diameter (see sect. 3.2.1.b). Shape models are not checked for convexity, they are assumed to be convex.

3.2.1.a Outbound surface-normal vector

Each facet is defined by three vertex vectors $v_{1,2,3}^{\vec{}}$ and has an outbound surface-normal vector (normal to the facet with a modulus equal to the facet size)

$$\mathrm{d}\vec{\mathcal{A}} = \pm\frac{1}{2}\,(\vec{v_2} - \vec{v_1}) \times (\vec{v_3} - \vec{v_1}) \tag{3.1}$$

where $\times$ denotes the vector product. We calculate $\mathrm{d}\vec{\mathcal{A}}$ with the positive sign and then check the orientation; the sign is flipped if the resulting vector is inbound. Assuming that the origin of the coordinate system is inside the object[1] (which is true for all common distributions of shape models), $\mathrm{d}\vec{\mathcal{A}}$ is outbound if

$$\mathrm{d}\vec{\mathcal{A}} \cdot \frac{\vec{v_1} + \vec{v_2} + \vec{v_3}}{3} > 0$$

(note that the division by 3 is not required to perform this test and is therefore not done in the code).

3.2.1.b Intrinsic diameter

So far, all linear dimensions are in unspecified units. To convert them into physical units, they must be multiplied with a scale factor

$$s := \frac{D_{\mathrm{phys}}}{D_{\mathrm{intr}}} \tag{3.2}$$

where D_{phys} is the physical diameter determined from the constant H and the variable p_{V} (eqn. 1.1), and D_{intr} is the intrinsic diameter of the shape model in unspecified units. As is common practice, the effective diameter is defined as that of the sphere of identical volume (see eqn. 2.1 on p. 28). The total volume V of the polyhedral shape model equals the sum of all tetrahedral volumes V_i defined

[1] Strictly speaking, the more stringent requirement holds that all straight lines connecting the origin to the vertices must entirely lie within the object. By the definition of convexity, this is implied if the origin is inside the object.

by the origin and the three vertices $v_{i,\vec{1}23}$ belonging to facet i

$$V = \sum_i \frac{1}{6} \left| (v_{i,\vec{1}} \times v_{i,\vec{2}}) \cdot v_{i,\vec{3}} \right| \tag{3.3a}$$

$$D_{\mathrm{intr}} = \sqrt[3]{\frac{6V}{\pi}}. \tag{3.3b}$$

The scale factor s is updated inside the TPM code whenever the variable p_{V} is updated.

3.2.1.c Transformation into a co-rotating system

For the calculation of model fluxes, the coordinates of the Sun, $\vec{e_S}$, and of the observer, $\vec{e_O}$, in a co-rotating asteroid-centric coordinate system are required. They are calculated from the epoch of the observation, t, and from the ecliptic coordinates of the asteroid in heliocentric (λ_S, β_S) and observer-centric (λ_O, β_O) frames, respectively, which are typically taken from ephemeris generators. Further required input parameters are the epoch of zero rotational phase JD_0, the spin period $\mathcal{P}$, and the ecliptic coordinates of the spin axis (λ_A, β_A). The transformation into the bodycentric co-rotating system reads: ($R_a(\phi)$ denotes the counter-clockwise rotation about the a axis by the angle ϕ in radians)

$$-\vec{e_x} = R_z\left(-(t-\mathrm{JD}_0)\,\frac{2\pi}{P}\right) R_y\left(\beta_A - \frac{\pi}{2}\right) \begin{pmatrix} \cos(\lambda_x - \lambda_A)\cos\beta_x \\ \sin(\lambda_x - \lambda_A)\cos\beta_x \\ \sin\beta_x \end{pmatrix} \tag{3.4}$$

using the usual Euler rotations (substitute S or O for x; the first Euler rotation is performed explicitly, leading to the longitude $\lambda_x - \lambda_A$); the minus sign in front of $\vec{e_x}$ reflects the fact that ephemeris coordinates denote vectors pointing towards the asteroid, whereas in the following we require vectors pointing away from it.

3.2.2 Thermal conduction

Thermal conduction into and from the subsoil causes asteroids to display thermal inertia (see sect. 2.2.2), such that their surface temperatures not only depend on the instantaneous insolation but also on the thermal history. As will be discussed in sect. 3.2.2.b, the thermal inertia of asteroid surfaces may vary by some two orders of magnitude, depending on various surface properties, leading to significant differences in surface temperatures and hence in thermal fluxes.

As is common practice, lateral heat conduction is neglected; the length scale of thermal conduction phenomena, the skin depth l_S, is typically in the cm-range, much below the resolution of available asteroid shape models.

Like most authors of recent asteroid thermophysical models (see, e.g., Lagerros, 1996, 1998a; Delbo', 2004; Wright, 2007) we follow the example of Spencer et al. (1989) and assume all relevant thermal parameters to be constant with depth and hence with temperature (see discussion below).

3.2.2.a Mathematical description

Thermal conduction can be described in terms of the vector-valued heat flux, $\vec{\Phi}$, which is defined as the amount of heat transfer per cross-sectional area. $\vec{\Phi}$ points into the direction of the heat transfer, which is proportional to the gradient of the temperature T

$$\vec{\Phi} = -\kappa\vec{\nabla}T. \tag{3.5}$$

κ is a material specific constant, the *thermal conductivity.* Inside a thermal conductor, the thermal energy per unit volume reads ρcT, with the surface bulk mass density, ρ,[2] and the specific heat, c. By conservation of energy, local changes in thermal energy act as sources of heat flux, i.e.:

$$\frac{\partial}{\partial t}\rho cT = \vec{\nabla}\cdot\kappa\vec{\nabla}T. \tag{3.6}$$

In the case of opaque atmosphereless bodies such as asteroids, a boundary condition of this partial differential equation of second order stems from the absorption of solar flux at the surface (see eqn. 2.5 on p. 36)[3]

$$\epsilon\sigma T^4 = (1-A)\frac{S}{r^2}\mu_S + \Phi_N \tag{3.7}$$

where Φ_N is the heat flux projection onto the outbound surface normal, and μ_S is the cosine of the local zenith distance of the Sun (μ_S is defined to vanish when the Sun is below local horizon).[4] Thermal conduction thus couples surface

[2] ρ should not be confused with the total bulk mass density of the body which can be very different from that of the surface, e.g. in the case of loose regolith covering solid rock.

[3] Note that non-opaque materials, such as water ice, allow sunlight to be absorbed at non-negligible depth leading to, e.g., the solid-state greenhouse effect (see Kaufmann et al., 2006, 2007, and references therein).

[4] For the sake of compactness, we consider direct insolation as the only source of absorbed incoming flux throughout this section; other sources (originating, e.g., from other facets inside concavities such as craters) are straightforward to add to the solar-radiation term. Similarly,

temperatures to the sub-surface temperature profile.

Throughout this work, three approximations are made:

Constant thermal conductivity The thermal conductivity κ is assumed to be spatially constant, which tacitly includes that κ be temperature independent (otherwise $\vec{\nabla}\kappa = \partial\kappa/\partial T\,\vec{\nabla}T$, see the discussion in sect. 3.2.2.b). Under this assumption, eqn. 3.6 reduces to the well-known diffusion equation

$$\frac{\partial}{\partial t}T = \frac{\kappa}{\rho c}\Delta T. \tag{3.8}$$

with the Laplace operator $\Delta = \vec{\nabla}\cdot\vec{\nabla}$.

One-dimensional heat flow As we will see below, thermal conduction on asteroids is effective over typical length scales in the cm-range, significantly below the resolution of known shape models. We can therefore neglect lateral heat conduction and only consider one-dimensional heat flow into and from the subsoil. Throughout this work, a coordinate system will be used in which the Z axis coincides with the local surface normal, $Z = 0$ at the surface and $Z > 0$ below the surface.

No seasonal effects The insolation (and hence the temperature) on asteroids has typically two fundamental periods, the spin period $\mathcal{P}$ and the orbital period $\mathcal{T}$, leading to diurnal and seasonal effects, respectively. Typically, $\mathcal{T} \gg \mathcal{P}$. As will be seen below, seasonal effects are typically negligible on asteroids. Insolation and temperature are then periodic in time with period $\mathcal{P} =: 2\pi/\omega$.

Under these assumptions, it is possible to express all relevant quantities in a dimensionless way, following Spencer et al. (1989):

$$\tau = \omega t \tag{3.9a}$$

$$z = Z/l_S \tag{3.9b}$$

$$u = T/T_{SS} \tag{3.9c}$$

with the following definitions of skin depth l_S, subsolar temperature T_{SS}, thermal

shadowing can easily be incorporated by defining μ_S to vanish whenever the facet is shadowed.

inertia Γ, and thermal parameter Θ:

$$l_S = \sqrt{\frac{\kappa}{\omega\rho c}} \tag{3.10a}$$

$$T_{SS} = \sqrt[4]{\frac{(1-A)S/r^2}{\epsilon\sigma}}. \tag{3.10b}$$

$$\Theta = \frac{\kappa/l_S}{\epsilon\sigma {T_{SS}}^3} = \sqrt{\omega}\frac{\Gamma}{\epsilon\sigma {T_{SS}}^3} \tag{3.10c}$$

$$\Gamma = \sqrt{\kappa\rho c} \tag{3.10d}$$

Eqn. 3.8 and eqn. 3.7 acquire the form

$$\frac{\partial}{\partial\tau}u(z,\tau) = \frac{\partial^2}{\partial z^2}u(z,\tau) \tag{3.11a}$$

$$u(0,\tau)^4 = \mu_S(\tau) + \Theta\frac{\partial}{\partial z}u(0,\tau). \tag{3.11b}$$

The heat transfer problem depends solely on the thermal parameter, Θ, which is proportional to the thermal inertia, Γ, and otherwise independent of thermal properties. It is easily seen that $\Theta = 0$ corresponds to vanishing thermal inertia (c.f. eqn. 2.5) while $\Theta \to \infty$ corresponds to an FRM-like asteroid (c.f. eqn. 2.9). Θ is proportional to $1/\sqrt{\mathcal{P}}$, so the FRM limit is approached by fast rotators.

Equation eqn. 3.11a is a partial differential equation of second order which requires two suitable boundary conditions to be solvable: Eqn. 3.11b and the requirement that the temperature be spatially constant at infinite depth

$$\lim_{z\to\infty}\frac{\partial}{\partial z}u(z,\tau) = 0. \tag{3.12}$$

Since the surface boundary condition is τ periodic with period 2π, so must the solution $u(z,\tau)$, and there is a unique solution to the diffusion equation eqn. 3.11 in combination with eqn. 3.12, namely the wave equation [5]

$$u\left(z,\tau\right) = u_0 + \sum_{n=1}^{\infty} u_n \exp\left(-z\sqrt{n/2}\right)\cos\left(n\tau - z\sqrt{n/2} - \phi_n\right). \tag{3.13}$$

[5] Derivation: A solution of the partial differential equation eqn. 3.11 $u(z,\tau) \in \mathbb{R}$ with time period 2π can be Fourier decomposed (see, e.g., Wesselink, 1948)

$$u(z,\tau) = \sum_{n\in\mathbb{Z}} a_n \exp(in\tau) g_n(z) \qquad \forall_n\forall_z : a_n g_n(z) = \overline{a_{-n} g_{-n}(z)}$$

where $\overline{z}$ denotes the complex conjugate of z. Denoting derivatives w.r.t. z with primes we

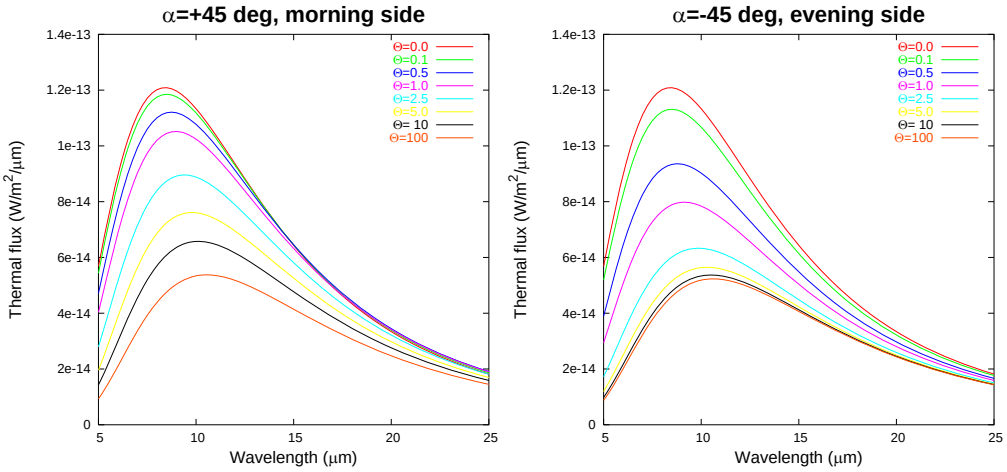

Figure 3.1: Thermal model spectra of a spherical smooth NEA for different values of Θ, which is proportional to thermal inertia Γ, and for phase angles of $\alpha = \pm 45°$, placing the sub-observer point at local times of 9 AM and 3 PM, respectively (Sun and observer are above the equator). Note the large *morning-evening* asymmetry for intermediate Θ values, which asymptotically vanishes for low and large Θ values. This asymmetry drives the important Yarkovsky effect (see sect. 1.3) and facilitates determinations of thermal inertia from thermal data despite the competing effect of thermal-infrared beaming which does not display a morning-evening asymmetry. Model parameters are $r = 1.1$ AU, $\Delta = 0.1$ AU, $\mathcal{P} = 6$ h, $A = 0.1$, and $\epsilon = 0.9$. Hence, $\Theta = 1$ corresponds to $\gamma \sim 160$ J s$^{-1/2}$K^{-1}m^{-2}. A typical value for NEAs is 300 J s$^{-1/2}$K^{-1}m^{-2} (see sect. 7.3).

The parameters u_n and ϕ_n remain to be determined from the surface boundary condition eqn. 3.11b. In practice, this is less convenient than a straightforward numerical integration of the differential equation, so the heat-wave solution is of little practical use. It is, however, important to realize that the amplitude of the heat wave decays exponentially with depth.

3.2.2.b Physical discussion

When observing the effect of thermal conduction on asteroid thermal fluxes, the primary observable quantity is Θ (see eqn. 3.10c). As can be seen from Fig. 3.1,

---

get:

$$n = 0: \quad g_0''(z) = 0 \qquad \longrightarrow g_0(z) = \lambda_0\, z + u_0$$

$$n > 0: \quad g_n''(z) = i n g_n(z) \quad \longrightarrow g_n(z) = \lambda_n \exp\left[\sqrt{n/2}\,(1+i)\,z\right] + \mu_n \exp\left[-\sqrt{n/2}\,(1+i)\,z\right]$$

$$n < 0: \quad g_n''(z) = i n g_n(z) \quad \longrightarrow g_n(z) = \lambda_n \exp\left[\sqrt{-n/2}\,(1-i)\,z\right] + \mu_n \exp\left[-\sqrt{-n/2}\,(1-i)\,z\right]$$

with constants λ_n and μ_n. The boundary condition eqn. 3.12 requires all λ_n to vanish. The proof is finished by substituting $a_n \mu_n(z)$ with $u_n \exp(i\phi_n)/2$ ($\forall_n : u_n \in \mathbb{R}$ and $\phi_n \in \mathbb{R}$).

Θ is difficult to measure in the limiting cases when it approaches 0 or ∞, and is most readily measurable for intermediate values of the order of 1.

Depending on their angular spin velocity ω and the subsolar temperature T_{SS} (which depends chiefly on the heliocentric distance r), objects with identical thermal inertia may nevertheless have very different thermal parameters. While it is intuitively clear that the surface temperatures of fast rotators are more significantly influenced by thermal conduction than those of cold rotators, the dependence of Θ on T_{SS} is less intuitively obvious; to explain the latter, it is instructive to think of thermal emission into space (proportional to ${T_{SS}}^4$) as a heat transfer mechanism which competes with conduction into the subsoil (proportional to T_{SS}). This explains, among other things, why the STM (which assumes $\Theta = 0$) appears to be a poor thermal model for Kuiper belt objects (see Stansberry et al., 2007, and references therein) despite the low thermal inertia typically expected for such objects: Due to their large heliocentric distances, Kuiper belt objects are cold, and hence Θ can no longer be neglected even for low Γ values.

The three physical parameters ρ, c, and κ cannot be determined separately, but only the thermal inertia $\Gamma = \sqrt{\rho c \kappa}$ (see eqn. 3.10d). As can be seen from table 3.1 on p. 58, for plausible asteroid-surface materials κ is much more variable than ρ and c, hence Γ is largely determined from κ. Γ is often transformed into κ and vice-versa assuming typical values of ρ and c. Confusingly, it is common practice among modelers of the Yarkovsky and YORP effects to consider κ as the primary variable (see, e.g., Bottke et al., 2006, and references therein; "thermal inertia" is often not mentioned in such papers), while thermal observers and modelers tend to highlight Γ rather than κ.

Geological interpretation As can be seen in table 3.1 on p. 58, the thermal inertia of lunar regolith is around 50 J $s^{-1/2}K^{-1}m^{-2}$, roughly that of very light polystyrene foam. Other plausible soil materials, such as coal or sand, have much larger thermal inertia, and bare rock (granite or marble) reaches $\Gamma \sim 2500$ J $s^{-1/2}K^{-1}m^{-2}$, some 50 times larger than that of lunar regolith. Metals are excellent thermal conductors, metallic meteoroids may therefore display a very large thermal inertia some 350 times larger than that of lunar regolith.

The thermal inertia of a given particulate material decreases with decreasing grain size unless grains are much larger than the thermal skin depth (see, e.g., Jakosky, 1986; Clauser, 1995; Presley and Christensen, 1997). Thermal inertia is thus a very sensitive indicator for the presence or absence of loose surface material.

Table 3.1: Thermal properties of some typical materials: thermal conductivity κ, mass density ρ, specific heat capacity c, all for temperatures of 20 °C unless otherwise stated. Thermal inertia Γ is calculated from eqn. 3.10d, skin depths l_S from eqn. 3.10a, assuming periods of $\mathcal{P} = 24$ h or 365 d. References: Text books and standard tables (Stephan, 2001; Volger and Laasch, 1989; Berber et al., 1999; Ahrendts, 2000), and Winter and Krupp (1971) for lunar regolith. Values in parentheses were estimated based on similar materials.

Material	κ W K^{-1}m^{-1}	ρ kg m^{-3}	c J kg^{-1}K^{-1}	Γ J s$^{-1/2}$K^{-1}m^{-2}	l_S (day) cm	l_S (year) cm
Nickel	91	8850	448	$19 \cdot 10^3$	56	1000
Iron	81	7860	452	$17 \cdot 10^3$	56	1000
Granite	2.9	2750	890	2600	13	250
Marble	2.8	2600	800	2400	14	260
Water ice, 0 °C	2.25	917	2000	2040	13	252
Water, 0 °C	0.56	1000	4200	1500	4.3	82
Snow (compact)	0.46	560	2100	740	7.3	140
Sandy soil	0.27	1650	800	600	5.3	100
Coal	0.26	1350	1260	665	4.6	88
Pumice	0.15	800	(900)	330	5.4	100
Paper	0.12	700	1200	320	4.4	85
Polystyrene foam	0.03	50	1500	47	7.4	140
Air, 20 °C	0.026	1.2	1000	5.6	55	1000
Lunar regolith	0.0029	1400	640	51	0.7	13

Note: *The entry for air only applies to small volumes of air, where convective heat transfer (which dominates in large volumes) is inefficient. For very porous bodies on Earth (such as polystyrene foam), heat conduction through air trapped inside the pores is the dominant heat transfer mechanism, placing a lower limit on thermal conductivity. On atmosphereless bodies such as the Moon or asteroids, lower conductivities are possible.*

This is widely used in Martian geology (see, e.g., Mellon et al., 2000; Christensen et al., 2003; Putzig et al., 2005, and references therein). It must be noted, however, that even the thin Martian atmosphere greatly enhances the thermal conduction among fine grains (see Presley and Christensen, 1997) relative to purely radiative heat transfer. To the best of our knowledge, the dependence of thermal inertia on grain size in a vacuum has not been studied so far, therefore it is presently not straightforward to interpret thermal-inertia values on asteroids in terms of grain size.

Another trend apparent in table 3.1 is that thermal inertia decreases with porosity (see the difference between ice and snow or the low thermal inertia of volcanic pumice). It is therefore hard to tell *a priori* what thermal inertia an asteroid composed of "bare rock" should display, but the commonly quoted value of 2,500 J s$^{-1/2}$K^{-1}m^{-2} (see the values for granite and marble in table 3.1) may be expected to be an upper limit.

It is also apparent from table 3.1 that neglecting lateral heat conduction on

asteroid surfaces is unlikely to introduce significant systematic uncertainties: Even metallic objects with their huge thermal inertia and with a relatively slow rotation rate of 24 h would have a thermal skin depth of only 56 cm, such that for all objects larger than a few tens of meters in diameter lateral heat conduction can be safely neglected. However, lateral heat conduction is very important for thermal modeling of the precursor bodies of metallic meteoroids and their Yarkovsky drifts. Since such objects cannot be observed with current mid-IR telescopes, they are beyond our scope.

Heat transfer mechanisms There are three major heat transfer mechanisms: conduction, convection, and thermal radiation. While convection is irrelevant on atmosphereless bodies, both conductive and radiative heat transfer could plausibly occur on asteroids. Conduction would be expected to occur within surface grains, while radiation should dominate the heat transfer between grains. In the limit of point-like grains, conduction vanishes while for compact bodies radiative heat transfer can be neglected. The relative importance of the two heat transfer processes thus depends on the typical surface-grain size, which is unknown for asteroids.

For conductive heat transfer, κ is largely independent of temperature T (for the materials and the temperature range relevant for our purposes) whereas radiative heat transfer is well described with $\kappa \propto T^3$. For lunar regolith, it is known from Apollo *in-situ* measurements and laboratory analysis of returned lunar samples that both conductive and radiative heat transfer are relevant, such that $\kappa = a+bT^3$ with constants a and b (see, e.g., Jones et al., 1975, and references therein; in their model, a and b are functions of depth).

Kührt and Giese (1989) proposed a complex TPM in which lunar results are rescaled to the conditions prevailing on the Martian satellites. When attempting to use their model to fit observational data of Deimos and Phobos, however, they reverted to a simplified model, in which only the radiative T^3 term is considered (Giese and Kührt, 1990; Kührt et al., 1992). Note that in this case heat transfer is no longer described by the diffusion equation eqn. 3.8 on p. 54, but an additional term occurs, which stems from the derivative of κ.

Most TPMs for asteroids proposed so far assume Γ to be independent of depth and temperature (see Spencer et al., 1989; Lagerros, 1996; Delbo', 2004; Wright, 2007, and references therein). This implicitly prefers conductive over radiative heat transfer. Another, widely quoted, interpretation is that the exact dependence

of thermal parameters on depth and temperature is too poorly constrained by available data to be modeled explicitly, hence one reverts to constant values which are effective averages over the relevant length scales.

Due to their generally lower heliocentric distance, NEAs are typically hotter than MBAs, hence one might expect the radiative T^3 term to be more important for their thermal emission than for that of MBAs. However, the relative importance of the T^3 radiative term and the T^0 conductive term are not clear *a priori*. An "Apollo-like" thermal conductivity model with two or more fit parameters (a and b given above) would probably be most realistic, but the ratio a/b would be very hard to constrain with typical asteroid data. We adopted a model in which all thermal properties including κ are assumed to be constant, but we note that it may be worthwhile to consider a model in which κ is proportional to T^3. This is left to future work.

3.2.3 Thermal-infrared beaming

As introduced in sect. 2.2.3, the emission characteristics of asteroids surfaces are different to those of smooth Lambertian surfaces, with an observed relative temperature and flux enhancement at low phase angles which, due to conservation of energy, must correspond to relative flux losses at large phase angles. This phenomenon is referred to as *thermal-infrared beaming* and is well known from thermal observations of the Moon (see, e.g., Saari and Shorthill, 1972, for an overview) and Mercury (e.g. Emery et al., 1998). The surfaces of these bodies are well known to be densely covered with impact craters; "cratered" thermophysical models were seen to reproduce the observed beaming well (see, e.g., Buhl et al., 1968; Winter and Krupp, 1971; Emery et al., 1998). In these models, craters are modeled as sections of hemispheres and the beaming effect stems from *mutual heating* of facets due to reabsorption of scattered and thermally emitted flux inside the crater, and furthermore from *shadowing* effects which become relevant at large phase angles, both leading to sharp temperature contrasts on small length scales.

Similar crater models have been successfully applied to planetary satellites (e.g. Giese and Kührt, 1990; Kührt et al., 1992) and are frequently employed to model asteroid surface roughness (see Hansen, 1977; Spencer, 1990; Lagerros, 1998a; Delbo', 2004, and references therein).

These models differ in the degree to which multiple scattering inside craters is taken into account: While Hansen (1977) neglect multiple scattering altogether but include shadowing and mutual heating due to reabsorption of thermal flux,

Spencer (1990) additionally considers multiple scattering of sunlight but not of thermal flux (equivalently, $\epsilon = 1$ is assumed inside craters); Delbo' (2004) follows Spencer's approach. The crater model by Kührt and Giese (1989) is virtually identical to Spencer's but differs in the treatment of thermal conduction inside craters (see below). The model by Lagerros (1998a) is the most complete crater model currently available: Direct and multiply scattered sunlight, shadowing, and reabsorption and multiple scattering of thermal radiation are taken into account. We here present an improvement over the model by Lagerros (1998a) where multiple thermal scattering is fully considered to all orders (see sect. 3.2.3.e for our improvement to Lagerros' model).

Several methods have been proposed in the literature to model thermal conduction inside hemispherical craters. Lagerros (1998a) and Delbo' (2004) explicitly solve the one-dimensional heat conduction problem for each surface tile inside the crater (see above for limitations of the Delbo', 2004, model) which is, however, computationally very expensive. Although a more complex model had been proposed by Kührt and Giese (1989), the same authors used a simplified variant thereof for fitting observations of the Martian satellites (Giese and Kührt, 1990; Kührt et al., 1992), in which effectively only one subsoil depth is considered—while this satisfactorily reproduces the effect of thermal inertia on the diurnal lightcurve amplitude, it fails to reproduce the phase lag introduced by thermal inertia. We use an approximation proposed and validated by Lagerros (1998a) (see sect. 3.2.3.f) in which the numerical treatment of thermal conduction and cratering decouple, which is numerically highly advantageous.

3.2.3.a Model assumptions

Beaming is modeled by adding craters to each surface facet. Variable model parameters are the crater opening angle (equivalent to the relative crater depth) and the crater density, i.e. the surface fraction covered in craters. Very small craters with diameters comparable to or below the thermal skin depth l_S (in the cm-range for typical asteroid surfaces, see table 3.1 on p. 58) do not contribute significantly to the observable beaming because temperature contrasts are reduced by lateral heat conduction. We shall only consider much larger craters, such that lateral heat conduction can be neglected. Under this assumption, thermal fluxes are independent of the crater size distribution for a given opening angle and crater density. One-dimensional heat conduction inside craters is considered in an approximate way, which decouples the treatment of craters from that of thermal conduction.

Multiple scattering and reemission of both sunlight and thermal emission are fully taken into account, our approach is an improvement over that by Lagerros (1998a), the most complete available in the literature so far. So far, the only considered source of input flux is the Sun; for globally non-convex asteroid shapes, where facets may receive additional flux from one another, a generalized model may be required (see sect. A.1.5 on p. 251).

Two different radiation fields inside the crater are considered, one at optical wavelengths with total energy density $J_V(\vec{r})$ and corresponding absorptivity $1-A$ (A denotes the bolometric Bond albedo); and another radiation field $J_{IR}(\vec{r})$ containing thermal radiation (integrated over all thermal wavelengths), with spectrally constant emissivity = absorptivity ϵ and reflectivity $1-\epsilon$. These two fields are independent from one another, with the exception that absorption of optical energy is a source of thermal energy.

3.2.3.b Geometry

Since the crater size distribution is irrelevant, the crater radius is set to unity without loss of generality. The crater shape then solely depends on the opening angle γ, where low γ corresponds to shallow craters and $\gamma = 180°$ corresponds to craters shaped as full hemispheres, the deepest craters considered. The slope of surface facets at the crater rim relative to neighboring smooth facets equals $\gamma/2$. Throughout the following, we use the following parametrization of the crater surface

$$\vec{r} = \begin{pmatrix} \sin\theta\cos\phi \\ \sin\theta\sin\phi \\ -\cos\theta \end{pmatrix} \tag{3.14}$$

where ϕ runs from 0–2π and θ from 0–$\gamma/2$. The crater floor is at depth -1, the crater rim at depth $-\cos(\gamma/2)$, hence the total crater depth is $1-\cos(\gamma/2)$. Note that in our notation the value of the opening angle is twice as large as in the notations of Kührt and Giese (1989); Spencer (1990); Emery et al. (1998); Delbo' (2004): in their notation, e.g., the full hemisphere has an opening angle of 90° rather than 180°. Hansen (1977) and Lagerros (1998a) parametrize crater shape in terms of depth over diameter S' [6] rather than opening angle γ; for comparison

[6] They use the symbol S which we replace by S' to avoid confusion with the solar constant.

the following expressions are helpful:

$$S' = \frac{1 - \cos(\gamma/2)}{2} = \sin^2\left(\frac{\gamma}{4}\right) \tag{3.15a}$$

$$1 - S' = \cos^2\left(\frac{\gamma}{4}\right). \tag{3.15b}$$

The outbound area element $\mathrm{d}\vec{\mathcal{A}}(\vec{r})$ inside the crater is given by

$$\mathrm{d}\vec{\mathcal{A}}\left(\vec{r}\right) = -\sin\theta\ \vec{r}\ \mathrm{d}\theta\ \mathrm{d}\phi, \tag{3.16}$$

in particular the outbound unit normal vector $\vec{n}$ equals

$$\vec{n}\left(\vec{r}\right) = -\vec{r}. \tag{3.17}$$

We make frequent use of the local directional cosines of the directions towards the Sun, $m_S(\vec{r})$, and the observer, $m_O(\vec{r})$; and of the cosines of the angular distances of Sun, μ_S, and observer, μ_O, from local zenith. All these quantities are clipped to be non-negative. Denoting the unit direction-vector towards the Sun or, respectively, the observer as r_x (substitute S or O for x) and the unit vector in z direction (i.e. local zenith) as $\vec{e_z}$, μ_x equals $\vec{r_x} \cdot \vec{e_z}$ (or 0 if $\vec{r_x}$ is below local horizon) and

$$m_x\left(\vec{r}\right) = \begin{cases} -\vec{r} \cdot \vec{r_x} & \text{if } \vec{r_x} \text{ is visible from } \vec{r} \\ 0 & \text{otherwise (i.e. } \vec{r} \text{ is eclipsed/occulted)} \end{cases} \tag{3.18}$$

$\vec{r_x}$ is visible from $\vec{r}$ if μ_x is positive and if the straight line containing $\vec{r}$ with tangent vector $\vec{r_x}$ intersects the sphere circumscribing the crater above the crater rim (in addition to the trivial intersection at $\vec{r}$ itself):

$$\vec{r} \cdot \vec{e_z} - 2\left(\vec{r} \cdot \vec{r_x}\right)\left(\vec{r_x} \cdot \vec{e_z}\right) > -\cos\left(\frac{\gamma}{2}\right). \tag{3.19}$$

The vectors $\vec{r_S}$ and $\vec{r_O}$ in the crater coordinate system can be constructed from scalar products performed in the asteroid-centric coordinate system (scalar prod-

ucts are invariant under rotations) which is computationally advantageous:

$$\vec{r_S} = \begin{pmatrix} \sqrt{1-{\mu_S}^2} \\ 0 \\ \mu_S \end{pmatrix} \tag{3.20}$$

$$\vec{r_O} = \begin{pmatrix} \sqrt{1-{\mu_O}^2}\cos\phi_A \\ \sqrt{1-{\mu_O}^2}\sqrt{1-\cos^2\phi_A} \\ \mu_O \end{pmatrix}. \tag{3.21}$$

The μ_x can be calculated from the scalar products of $\vec{r_x}$ and $\mathrm{d}\vec{\mathcal{A}}$ and

$$\cos\phi_A = \frac{\vec{r_S}\cdot\vec{r_O} - \mu_S\mu_O}{\sqrt{1-{\mu_S}^2}\sqrt{1-{\mu_O}^2}}. \tag{3.22}$$

(note that this approach fails when thermal conduction inside the crater is explicitly modeled, since then knowledge of $\vec{r_x}$ is required as a function of rotational phase).

Another important quantity in the following discussion is the *view factor* $V_{rr'}$ from $\vec{r}$ to $\vec{r'}$. It is defined as the fraction of radiative energy per area leaving the facet centered at $\vec{r}$ and directly striking that at $\vec{r'}$. Assuming Lambertian emission, the view factor is a purely geometric quantity symmetric in $\vec{r}$ and $\vec{r'}$; it equals

$$V_{rr'} = \frac{\left(\vec{n}\cdot\left(\vec{r'}-\vec{r}\right)\right)\left(\vec{n'}\cdot\left(\vec{r}-\vec{r'}\right)\right)}{\pi\left|\vec{r}-\vec{r'}\right|^4} \tag{3.23}$$

with the unit outbound surface-normal vectors $\vec{n}$ and $\vec{n'}$. In particular, the solid angle under which a facet is visible at another is proportional to the product of its size and the view factor. Inside a sphere, $\vec{n} = -\vec{r}$ (see eqn. 3.17), hence (using $\vec{r}\cdot\vec{r} = \vec{r'}\cdot\vec{r'} = 1$)

$$V_{rr'} = \frac{(\vec{r}\cdot(\vec{r'}-\vec{r}))(\vec{r'}\cdot(\vec{r}-\vec{r'}))}{\pi\left|\vec{r}-\vec{r'}\right|^4} = \frac{1}{4\pi}. \tag{3.24}$$

The fact that the view factor is constant is a peculiarity of the sphere owing to its high symmetry; it will prove to be crucial in the following. In particular, it

enables the analytic evaluation of two important surface integrals:

$$\int_{\mathcal{A}} V_{rr'} \mathrm{d}\mathcal{A} = \frac{2\pi}{4\pi} \int_0^{\gamma/2} \sin\theta \mathrm{d}\theta = \frac{1-\cos(\gamma/2)}{2} = \sin^2\left(\frac{\gamma}{4}\right) \tag{3.25}$$

and

$$\int_{\mathcal{A}} V_{rr'} m_x\left(\vec{r}\right) \mathrm{d}\mathcal{A} = \mu_x \sin^2\left(\frac{\gamma}{4}\right) \cos^2\left(\frac{\gamma}{4}\right). \tag{3.26}$$

Proof of eqn. 3.26. By construction, the integral over the entire crater $\mathcal{A}$ equals the integral over that part $\mathcal{A}'$ from which $\vec{r_x}$ is not obstructed because $m_x(\vec{r})$ vanishes elsewhere. On $\mathcal{A}'$, the integral can be written as $\frac{1}{4\pi}\int_{\mathcal{A}'} \vec{r_x} \cdot \mathrm{d}\vec{\mathcal{A}'}$ (see eqn. 3.17 and 3.18) which, by virtue of Gauss' theorem, equals the sum of three contributions:

1. the integral over the crater "cap" $= \frac{2\pi}{4\pi}\mu_x \int_0^{\sin(\gamma/2)} \rho \mathrm{d}\rho = \mu_x/4 \sin^2(\gamma/2) = \mu_x \sin^2(\gamma/4)\cos^2(\gamma/4)$

2. the vanishing integral over the "terminator," i.e. the boundary between volume elements that see or do not see $\vec{r_x}$. The surface normal vector of that region is perpendicular to $\vec{r_x}$ by construction, hence this integral vanishes (if the entire crater sees $\vec{r_x}$, this integral vanishes trivially)

3. the volume integral of the (vanishing) divergence of $\vec{r_x}$ inside the region circumscribed by the three areas.

□

3.2.3.c Optical flux

A necessary prerequisite to the determination of the temperature distribution inside the crater is a complete knowledge of the radiation field at optical wavelengths $J_V(\vec{r})$. Apart from direct insolation, surface elements receive scattered light from other facets, where multiple scattering occurs, i.e. light scattered from one facet to another may be scattered again at the latter.

There are two approaches to model multiple scattering, either by summing up individual scattering orders (which we will do at the end of this section for

illustrative purposes) or by self-consistency, i.e. by solving the integral equation

$$J_V(\vec{r}) = A\left[\frac{S}{r^2}m_S(\vec{r}) + \int\limits_{\mathcal{A}'} J_V(\vec{r'})V_{rr'}\mathrm{d}\mathcal{A}'\right], \tag{3.27}$$

with solar constant S and heliocentric distance r (in AU). Eqn. 3.27 can be solved analytically for hemispherical craters because the view factor $V_{rr'}$ is constant (see eqn. 3.24), hence the integral in eqn. 3.27 is independent of $\vec{r}$, i.e. a mere constant K_1

$$J_V(\vec{r}) = A\left[\frac{S}{r^2}m_S(\vec{r}) + K_1\right]. \tag{3.28a}$$

$$K_1 = \int\limits_{\mathcal{A}'} J_V(\vec{r'})\frac{\mathrm{d}\mathcal{A}'}{4\pi} = A\left[\frac{S}{r^2}\int\limits_{\mathcal{A}'} m_S(\vec{r})\frac{\mathrm{d}\mathcal{A}'}{4\pi} + K_1\int\limits_{\mathcal{A}'}\frac{\mathrm{d}\mathcal{A}'}{4\pi}\right] \tag{3.28b}$$

by reinserting eqn. 3.27. Using the integrals eqn. 3.25 and 3.26:

$$K_1 = A\left[\frac{S}{r^2}\mu_S \sin^2\left(\frac{\gamma}{4}\right)\cos^2\left(\frac{\gamma}{4}\right) + K_1\sin^2\left(\frac{\gamma}{4}\right)\right] \tag{3.29a}$$

$$K_1 = A\mu_S\frac{S}{r^2}\frac{\sin^2(\gamma/4)\cos^2(\gamma/4)}{1 - A\sin^2(\gamma/4)} \tag{3.29b}$$

such that

$$J_V(\vec{r}) = A\frac{S}{r^2}\left[m_S(\vec{r}) + \mu_S\frac{\sin^2(\gamma/4)\cos^2(\gamma/4)}{1 - A\sin^2(\gamma/4)}\right]. \tag{3.30}$$

Correction of the Bond albedo The presence of craters lowers the albedo relative to that of a flat surface patch. Due to the absorption processes associated with multiple scattering, the crater scatters less optical flux outward than a flat surface of equal area would. The corrected Bond albedo A_{corr} equals $V_{\mathrm{out}}/V_{\mathrm{in}}$ with total in- and outgoing optical flux V_{in} and V_{out}, respectively.[7] The total solar flux V_{in} entering through the crater rim equals $\mu_S S/r^2$ times the projected area of the crater cap $\pi\sin^2(\gamma/2) = 4\pi\sin^2(\gamma/4)\cos^2(\gamma/4)$. The total outgoing flux V_{out} equals $\int_{\mathcal{A}'}\int_{\mathcal{A}} J_V(\vec{r'})V_{rr'}\mathrm{d}\mathcal{A}\mathrm{d}\mathcal{A}'$, where the integral is performed over the crater interior $\mathcal{A}'$ and the crater cap $\mathcal{A}$. By virtue of Gauss' theorem, one can deform $\mathcal{A}$ into the complement of the sphere circumscribing the crater (i.e. the range

[7] In principle, this ratio must be averaged over the hemisphere of all possible incidence directions. Below, however, we will find the albedo to be independent of the incidence angle.

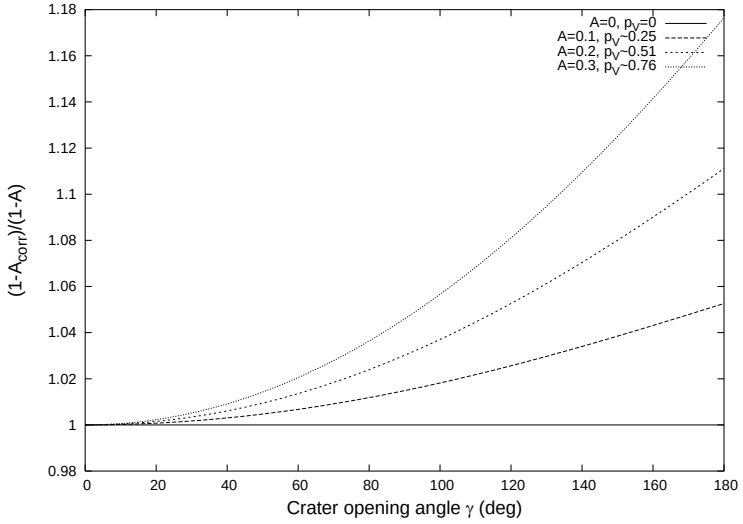

Figure 3.2: Dependence of absorptivity $1 - A$, which determines temperatures, on the albedo correction due to the presence of craters (see eqn. 3.31) as a function of crater opening angle γ for different values of flat-surface Bond albedo A. To convert A into geometric albedo p_V, $G = 0.15$ is assumed (see sect. 2.2.1).

$\gamma/2 < \theta < \pi$) without changing the result, such that

$$\begin{aligned} V_\mathrm{out} &= \int_0^{2\pi} \mathrm{d}\phi \int_{\gamma/2}^{\pi} \sin\theta \mathrm{d}\theta K_1 \qquad \text{(see eqn. 3.28)} \\ &= 2\pi \left(2\cos^2\left(\frac{\gamma}{4}\right)\right) A\mu_S \frac{S}{R^2} \frac{\sin^2(\gamma/4)\cos^2(\gamma/4)}{1 - A\sin^2(\gamma/4)} \\ &= V_\mathrm{in} A \frac{1 - \sin^2(\gamma/4)}{1 - A\sin^2(\gamma/4)} \end{aligned}$$

such that the corrected Bond albedo reads

$$A_\mathrm{corr} = A \frac{1 - \sin^2(\gamma/4)}{1 - A\sin^2(\gamma/4)}. \tag{3.31}$$

See Fig. 3.2 for a depiction of the relative changes in absorptivity $1 - A$. For realistic asteroid albedos $p_\mathrm{V} \leq 0.6$ (see sect. 1.5.1; $p_\mathrm{V} = 0.6$ corresponds to $A = 0.24$ assuming $G = 0.15$, see sect. 2.2.1), the relative change in absorptivity cannot greatly exceed 10 %, leading to only moderature changes in temperature since $T \propto \sqrt[4]{1 - A}$. It is, however, very important to use the corrected Bond albedo when verifying that the ingoing optical flux equals the total optical and thermal flux, which is an important test of model consistency used in the following.

Direct summation of scattered light to all orders It is instructive to verify eqn. 3.30 by explicitly summing up scattered contributions to all orders, which can be performed analytically in this case: For the sake of this discussion, let us denote the amount of directly scattered sunlight emanating from $\vec{r}$ as $J_0(\vec{r})$ and the n-times scattered component as $J_n(\vec{r})$. Then

$$J_V(\vec{r}) = \sum_{n=0}^{\infty} J_n(\vec{r}) \tag{3.32}$$

and the following relations hold:

$$\begin{aligned} J_0(\vec{r}) &= A\frac{S}{r^2} m_S(\vec{r}) \\ J_1(\vec{r}) &= A \int_{\mathcal{A}'} J_0(\vec{r'}) V_{rr'} \mathrm{d}\mathcal{A}' = A^2 \frac{S}{r^2} \mu_S \sin^2\left(\frac{\gamma}{4}\right) \cos^2\left(\frac{\gamma}{4}\right) \\ \forall_{n\geq 1} : J_{n+1}(\vec{r}) &= A \int_{\mathcal{A}'} J_n(\vec{r'}) V_{rr'} \mathrm{d}\mathcal{A}' = A \sin^2\left(\frac{\gamma}{4}\right) J_n(\vec{r}) \end{aligned}$$

(the middle equation holds because of eqn. 3.26 and, inductively, implies the third equation together with eqn. 3.25—note that all $J_n(\vec{r})$ are independent of $\vec{r}$ for $n \geq 1$). Eqn. 3.32 acquires the form of a geometric series and can be summed up analytically ($\sum_{n=0}^{\infty} q^n = 1/(1-q)$ for $|q| < 1$; here, $q = A\sin^2(\gamma/4) < 1$), yielding eqn. 3.30.

3.2.3.d Temperature distribution

Similar to the total optical flux $J_V(\vec{r})$, the total thermal flux emanating from $\vec{r}$, $J_{IR}(\vec{r})$, equals the sum of the locally emitted flux $\epsilon\sigma T^4(\vec{r})$ plus the flux scattered away from $\vec{r}$

$$J_{IR}(\vec{r}) = \epsilon\sigma T^4(\vec{r}) + (1-\epsilon) \int_{\mathcal{A}'} J_{IR}(\vec{r'}) V_{rr'} \mathrm{d}\mathcal{A}' \tag{3.33}$$

$$= \epsilon\sigma T^4(\vec{r}) + (1-\epsilon) K_2, \tag{3.34}$$

where, again, K_2 is constant because the view factor $V_{rr'}$ is constant. As above

$$K_2 = \int_{\mathcal{A}'} J_{IR}\left(\vec{r'}\right) V_{rr'} \mathrm{d}\mathcal{A}' = \epsilon\sigma \int_{\mathcal{A}'} T^4(\vec{r'}) \frac{\mathrm{d}\mathcal{A}'}{4\pi} + (1-\epsilon) K_2 \sin^2\left(\frac{\gamma}{4}\right)$$

$$K_2 = \frac{\epsilon\sigma}{1-(1-\epsilon)\sin^2(\gamma/4)} \int_{\mathcal{A}'} T^4(\vec{r'}) \frac{\mathrm{d}\mathcal{A}'}{4\pi}. \tag{3.35}$$

Sources of the temperature field $T(\vec{r})$ are absorption of direct sunlight, of scattered optical flux (see eqn. 3.30), of direct and scattered emission $J_{IR}(\vec{r})$ received from other facets, and thermal conduction from the subsoil:

$$\left(\frac{T(\vec{r})}{T_{SS}}\right)^4 = m_S(\vec{r}) + \int_{\mathcal{A}'} \left[(1-A)\frac{J_V(\vec{r'})}{\epsilon\sigma {T_{SS}}^4} + \epsilon \frac{J_{IR}(\vec{r'})}{\epsilon\sigma {T_{SS}}^4}\right] V_{rr'} \mathrm{d}\mathcal{A}' + \frac{\Theta}{T_{SS}} \frac{\partial T}{\partial z} \tag{3.36}$$

$$= m_S\left(\vec{r}\right) + \frac{1-A}{\epsilon\sigma {T_{SS}}^4} K_1 + \frac{\epsilon}{\epsilon\sigma {T_{SS}}^4} K_2 + \frac{\Theta}{T_{SS}} \frac{\partial T}{\partial z} \tag{3.37}$$

where the temperature derivative in the last term is with respect to the dimensionless depth coordinate of the one-dimensional heat-conduction problem considered in sect. 3.2.2, which is not to be confused with the z coordinate in the crater coordinate system. See eqn. 3.10b for the definition of the subsolar temperature T_{SS}.

If thermal inertia is explicitly modeled inside the crater, eqn. 3.37 takes the role of the surface boundary-condition eqn. 3.11b of the heat-conduction problem, which must be solved in conjunction with eqn. 3.35.

If thermal conduction is neglected inside craters, the last term in eqn. 3.37 vanishes, such that K_2 can be determined by inserting eqn. 3.37 and eqn. 3.29 into eqn. 3.35:

$$K_2 = \epsilon\sigma {T_{SS}}^4 \mu_S \frac{\sin^2(\gamma/4)}{1-A\sin^2(\gamma/4)} \qquad \text{neglecting thermal conduction} \tag{3.38}$$

and hence

$$\left(\frac{T\left(\vec{r}\right)}{T_{SS}}\right)^4 = m_S(\vec{r}) + \frac{\mu_S \sin^2\left(\gamma/4\right)}{1-A\sin^2\left(\gamma/4\right)} \left(\epsilon + A\cos^2\frac{\gamma}{4}\right). \tag{3.39}$$

This represents an analytic solution to the temperature distribution inside the crater, where multiple scattering of both sunlight and thermal asteroid radiation are taken into account to all orders (Lagerros, 1998a).

3.2.3.e Fluxes

The observable thermal flux $F(\lambda)$ at wavelength λ is the sum of the directly emitted flux component $F_0(\lambda)$ and an infinite number of scattered components $F_i(\lambda)$, where the index $i > 0$ denotes the scattering order

$$F(\lambda) = \sum_{i=0}^{\infty} F_i(\lambda).$$

Each of these components equals an integral of the respective local flux component $F_i(\lambda, \vec{r})$ over the visible portion of the crater. In particular

$$F_0(\lambda) = \int_{\mathcal{A}} \frac{m_O(\vec{r})}{\pi\Delta^2} F_0(\lambda, \vec{r})\, \mathrm{d}\mathcal{A} \tag{3.40a}$$

$$F_0(\lambda, \vec{r}) = \epsilon B(\lambda, T(\vec{r})) \tag{3.40b}$$

with the Planck function $B(\lambda, T)$ (see eqn. 2.6), the observer-centric distance Δ, and the local directional cosine towards the observer m_O (see eqn. 3.18). Scattered orders are determined recursively

$$F_{i+1}(\lambda) = \int_{\mathcal{A}} \frac{m_O(\vec{r})}{\pi\Delta^2} F_{i+1}(\lambda, \vec{r})\, \mathrm{d}\mathcal{A} \tag{3.41a}$$

$$F_{i+1}(\lambda, \vec{r}) = (1-\epsilon) \int_{\mathcal{A}} F_i(\lambda, \vec{r}) \frac{\mathrm{d}\mathcal{A}}{4\pi}, \tag{3.41b}$$

where we have used $V_{rr'} = 1/4\pi$ (eqn. 3.24). In particular

$$F_1(\lambda, \vec{r}) = (1-\epsilon) \int_{\mathcal{A}} \epsilon B(\lambda, T(\vec{r})) \frac{\mathrm{d}\mathcal{A}}{4\pi} \tag{3.42a}$$

$$F_1(\lambda) = (1-\epsilon) \int_{\mathcal{A}} \frac{m_O(\vec{r})}{\pi\Delta^2} \frac{\mathrm{d}\mathcal{A}}{4\pi} \int_{\mathcal{A}'} \epsilon B\left(\lambda, T\left(\vec{r'}\right)\right) \mathrm{d}\mathcal{A}' \tag{3.42b}$$

$$= (1-\epsilon)\mu_O \frac{\sin^2(\gamma/4)\cos^2(\gamma/4)}{\pi\Delta^2} \int_{\mathcal{A}} F_0(\lambda, \vec{r})\, \mathrm{d}\mathcal{A}. \tag{3.42c}$$

Observable flux according to Lagerros (1998a) In Lagerros (1998a), the total observable flux is approximated as the sum of directly emitted flux F_0 and singly

scattered flux F_1 (c.f. Lagerros, 1998a, eqn. 19),

$$F(\lambda)_{\text{Lagerros}} = F_0(\lambda) + F_1(\lambda) \tag{3.43a}$$

$$= \frac{\epsilon}{\pi\Delta^2} \int\limits_{\mathcal{A}} \left[m_O(\vec{r}) + \mu_O \sin^2\left(\frac{\gamma}{4}\right) \cos^2\left(\frac{\gamma}{4}\right) (1-\epsilon) \right] B\left(\lambda, T\left(\vec{r}\right)\right) \mathrm{d}\mathcal{A}. \tag{3.43b}$$

It is not discussed therein why higher scattering orders are neglected.

Observable flux to all orders While, to the best of our knowledge, this has not been discussed in the literature so far, it is feasible to consider *all* scattering orders in the calculation of observable flux. To this end it is crucial to realize that, because the view factor $V_{rr'} = 1/4\pi$ is constant, all scattered flux components $F_{i>0}(\lambda, \vec{r})$ are actually independent of $\vec{r}$ as is easily seen in the recursion eqn. 3.41. Hence

$$F_{i+1}\left(\lambda, \vec{r}\right) = (1-\epsilon) \int\limits_{\mathcal{A}} F_i\left(\lambda, \vec{r}\right) \frac{\mathrm{d}\mathcal{A}}{4\pi} = (1-\epsilon) \sin^2\left(\frac{\gamma}{4}\right) F_i\left(\lambda, \vec{r}\right) \tag{3.44}$$

for all $i \geq 1$ (using eqn. 3.25). The sum of all scattered flux components acquires the form of a geometric series

$$\sum_{i=1}^{\infty} F_i\left(\lambda\right) = F_1\left(\lambda\right) \sum_{i=0}^{\infty} \left[(1-\epsilon) \sin^2\left(\frac{\gamma}{4}\right) \right]^i = \frac{F_1\left(\lambda\right)}{1-(1-\epsilon)\sin^2(\gamma/4)} \tag{3.45}$$

and the flux to all orders reads

$$F(\lambda) = \sum_{i=0}^{\infty} F_i(\lambda)$$

$$= \frac{\epsilon}{\pi\Delta^2} \int\limits_{\mathcal{A}} \left[m_O(\vec{r}) + \frac{\mu_O (1-\epsilon) \sin^2(\gamma/4) \cos^2(\gamma/4)}{1-(1-\epsilon)\sin^2(\gamma/4)} \right] B\left(\lambda, T\left(\vec{r}\right)\right) \mathrm{d}\mathcal{A}. \tag{3.46}$$

Note, in particular, that the only difference between this expression and Lagerros' approximation (eqn. 3.43) is the redefinition of a constant factor, hence the effort to evaluate them through numerical integration is identical.

The difference between the two expressions is in second and higher scattering orders, i.e. of the order $(1-\epsilon)^2$. For asteroids, $\epsilon \sim 0.9$, this would be expected to lead to differences at the percent level, only. This has been verified numerically (see Fig. 3.3 on p. 72); only for rather unrealistically small ϵ values do the two

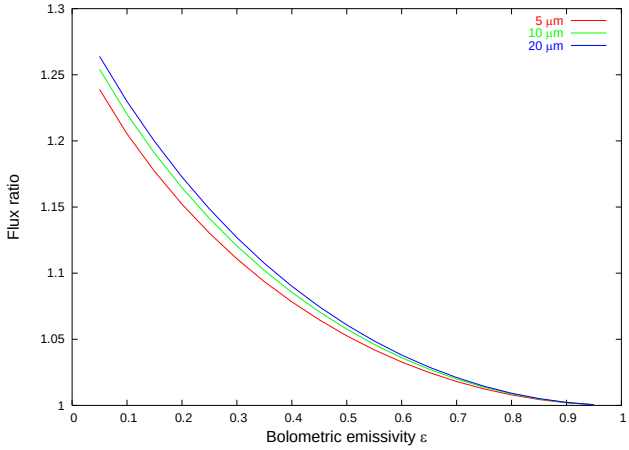

Figure 3.3: Ratio of crater model fluxes resulting from the solution to all scattering orders eqn. 3.46 relative to Lagerros' approximate treatment eqn. 3.43 as a function of ϵ. Both Sun and observer are at local zenith, used parameters are $\gamma = 180°$, $r = 1.1$ AU, $A = 0.1$. Model fluxes were determined using the code described in sect. 3.3.3.

expressions differ by more than 10 %.[8] However, since the effort in numerical evaluation is identical, there is no good reason *not* to use the full solution.

3.2.3.f Approximative treatment of thermal conduction inside craters

We do not explicitly model thermal conduction inside the crater, but rather use an approximation proposed by Lagerros (1998a, Eqn. 23). There, it is proposed that the relative temperature change due to thermal inertia inside the crater equals the relative temperature change outside the crater:

$$\frac{T_{\mathrm{crater}}(\Theta)}{T_{\mathrm{crater}}(0)} = \frac{T_{\mathrm{smooth}}(\Theta)}{T_{\mathrm{smooth}}(0)}. \tag{3.47}$$

Under this approximation, the numerical treatment of cratering decouples from that of thermal conduction. In particular, advantage can be taken of the analytic expression for the temperature distribution inside the crater neglecting thermal conduction (eqn. 3.39).

Lagerros (1998a) generated model fluxes using both his full-blown model and a simplified model making the approximation eqn. 3.47. He found that the latter systematically overestimates fluxes relative to the former, increasingly so with

[8] We have checked both solutions for conservation of energy as described in sect. 3.4.2. It was seen that the full solution does conserve energy to within numerical noise, while Lagerros' approximation does not—as expected, the mismatch increases systematically with decreasing ϵ and is insignificant for $\epsilon = 0.9$.

increasing crater opening angle and thermal parameter, but mutual agreement stayed within 1 % for the specific circumstances of his test.

While this is not discussed in Lagerros (1998a), the approximation eqn. 3.47 can not be used on the night side, where temperatures would vanish without thermal inertia. We therefore neglect craters on the night side altogether. For the same reason, temperature ratios diverge close to the terminator. Together with the finite spatial resolution of the shape models used by us, this leads to random occurrences of unphysically large flux contributions from facets close to the terminator. To prevent such overshoots, we clip the temperature ratio on the right-hand side of eqn. 3.47 to be ≤ 1.3; we have verified that model fluxes are largely independent of the precise value of this threshold value within reasonable limits.

3.3 Implementation

Our TPM model code has been implemented in C++. It compiles on a Windows XP platform using the compiler which is part of the Visual Studio .NET 2003 suite and furthermore under Linux using gcc. All debugging and testing has been performed under Windows.

In the code development, emphasis was put on a transparent, generic, and object-oriented code structure which makes it easy to add new features. Numerical efficiency was not a primary implementation goal. If in doubt, we erred on the side of simplicity and understandability as opposed to sophistication and obscurity. Not only does this save on development time (including time required for potential further development) but it also helps in the physical validation of the code. On the other hand, the model code is numerically quite inefficient, such that fits to large databases can require several nights of CPU time on a 2.66 GHz PC.

3.3.1 Class structure

The most important objects inherit from the abstract, generic base classes `asteroid` or `ThermalModelConvex` (the latter inherits from the more abstract `ThermalModel`).

`asteroid` is a purely abstract base class, only objects belonging to the sub-class `TriangulatedConvex` can be instantiated. Within its scope, all required information on the asteroid shape and spin state is stored, as well as the constants H, G, and ϵ. p_{V} is a `protected` variable within the scope of `asteroid`, its value can be changed using a routine which also updates the Bond albedo A and the diameter

scale factor s (since H is constant, changing p_V is equivalent to changing the diameter). `TriangulatedConvex` contains several routines to calculate disk-integrated thermal fluxes. These routines rely on `ThermalModelConvex` objects (see below) to calculate flux contributions from single facets; the actual model to be used is specified by passing a reference to the appropriate `ThermalModelConvex` object. The transformation of heliocentric and observer-centric asteroid coordinates into asteroid-centric directions towards the Sun or the observer (see sect. 3.2.1.c) is performed within the scope of `TriangulatedConvex`.

The chief interface between `asteroid` and `ThermalModelConvex` objects are the functions `fluxModFactors` and `ThermalLightCurveModFactors` within the scope of `ThermalModelConvex`. They return a dimensionless flux value or a dimensionless thermal lightcurve for a given time, observing geometry, and a single facet. All returned flux values must be multiplied by a constant factor of $2\pi\epsilon hc^2/(\Delta^2\lambda^5)\times s^2$ (with the scale factor s defined in eqn. 3.2 on p. 51) to convert them into units of W/m^2/µm. This multiplication is done by the calling routine within the scope of `asteroid` after adding contributions from all facets. `fluxModFactors` is overloaded to allow calculation of fluxes for either a single wavelengths or simultaneously for a vector of wavelengths, the latter significantly increases the efficiency if spectra are calculated for non-vanishing values of thermal inertia.

Important auxiliary classes include `ConvexFile`, `SpinState`, and `fitFileSI`. The latter serves to read in an ASCII file containing thermal flux values along with the epoch and observing geometry of the observations. All model flux values are in units of W/m^2/µm. The auxiliary class `fitFileMJy` is used to read in fit files with fluxes in units of mJy and to convert them into units of W/m^2/µm; `fitFileMJy` inherits from `fitFileSI`.

In order to fit thermal data, the TPM code is used to output ASCII files containing χ^2 for different combinations of thermal parameters which are then manually analyzed. Output files are in a suitable format for plotting using the open-source software `gnuplot`. For each combination of thermal parameters, a best-fit p_V is determined analogous to our NEATM-fitting approach (see eqn. 2.17 on p. 45). If the crater density is considered as a fit parameter, linear regression is used to analytically determine the best-fit crater density. χ^2 values are determined by calling an appropriate function at the `main`-routine level. Prior to this, the data file (or files) are read in and a `TriangulatedConvex` object is instantiated with all asteroid constants including the shape model (passed as a `ConvexFile` object) and the `SpinState`. Then, for each combination of relevant model parameters,

a `ThermalModelConvex` object is instantiated,[9] which is used to calculate model fluxes for the times and observing geometry given in the fit files.

3.3.2 Thermal conduction

The subclass of `ThermalModelConvex` for numerical modeling of thermal conduction on smooth surface elements is `ThermalInertiaOnlyConvex`. Thermal conduction is modeled as described in sect. 3.2.2. The dimensionless heat diffusion equation (eqn. 3.11) in the subsoil and the boundary condition at the surface (eqn. 3.11b) are discretized in a straightforward fully explicit way with equidistant sampling points in space and time. This is numerically stable provided the time resolution is not too coarse, specifically (see Press et al., 1992, sect. 19.2) the parameter `dTdZ2` (dimensionless time resolution divided by the square of the dimensionless depth resolution) must not exceed 0.5. The numerical integration is truncated at a certain depth, at which the infinite-depth boundary condition eqn. 3.12 is taken into account.

In the constructor, the thermal parameter and the desired fractional accuracy goal are specified as well as the discretization parameters `nTime` (number of time steps), `nZ` (number of depth steps), and `zMax` (maximum depth in units of skin depths). The constructor checks whether the stability criterion mentioned above is met and throws an exception otherwise.

To calculate surface temperatures, the cosine of the solar angular zenith distance μ_S, clipped to be non-negative, is determined for each time step and stored into an array. If all entries are essentially zero, zero flux is returned (the facet is not illuminated for any time of day). Then an array containing the temperature profile is initialized with a constant temperature distribution,[10] and the asteroid is spun until the surface temperature at the desired time has remained constant to within the user-specified fractional accuracy goal. For all time steps, the temperature profile is kept in the computer's RAM, which proved helpful for debugging and validating the code. An asteroid revolution consists of `nTime` time steps. For each, the new subsoil temperature profile `newP[i]` (with $1 \leq i \leq \mathtt{nZ} - 2$) is determined

[9] If thermal inertia is considered and if data were taken at more than one epoch, data from each epoch should be stored within a separate fit file, and separate `ThermalModelConvex` objects should be instantiated for each. Differences in heliocentric distance r translate into differences in thermal parameter Θ for otherwise constant parameters.

[10] It has been verified that the final surface temperature is independent of that initialization.

from the old profile `oldP[i]` using

$$\texttt{newP[i]} = \texttt{oldP[i]} + \texttt{dTdZ2}\,(\texttt{oldP[i-1]} + \texttt{oldP[i+1]} - 2\texttt{oldP[i]})\,, \qquad (3.48)$$

with the parameter `dTdZ2` defined above. The surface temperature `newP[0]` is determined from a discretization of the boundary condition (eqn. 3.11b)

$$\texttt{newP[0]}^4 = \mu_S + \Theta\frac{\texttt{newP[1]} - \texttt{newP[0]}}{\texttt{dZ}} \qquad (3.49)$$

with the dimensionless spatial resolution `dZ`. This nonlinear equation is solved using Newton's method, with `oldP[0]` as a first guess for `newP[0]`. The new temperature at the maximum depth considered, `newP[nZ-1]`, is calculated from eqn. 3.48 assuming that the fictitious `oldP[nZ]` equals `oldP[nZ-1]`, thus approximating the boundary condition at infinite depth (eqn. 3.12)

$$\texttt{newP[nZ-1]} = \texttt{oldP[nZ-1]} + \texttt{dTdZ2} * (\texttt{oldP[nZ-2]} - \texttt{oldP[nZ-1]})\,. \qquad (3.50)$$

Typically used values for `nZ`, `zMax`, and `nTime` are 25, 6, and 300, respectively, a typical value for the fractional accuracy goal is 0.0001.

The fully explicit discretization scheme used to solve the heat diffusion equation and the discretization of the boundary conditions are fully encapsulated within the scope of the class `ThermalInertia` and its member class `TimeStep`. Other discretization schemes, such as Crank-Nicholson (see, e.g., Press et al., 1992, sect. 19.2) can be implemented easily without changes to the remaining code.

3.3.3 Beaming

Without thermal inertia Fluxes are calculated by `HemisphericNoInertia` objects, which inherit from `ThermalModelConvex`. Returned fluxes are for a crater density of 100 % and must be combined with "non-cratered" fluxes in the calling function to account for lower crater densities.

The temperature distribution inside the crater follows from eqn. 3.39, fluxes are obtained by numerically integrating eqn. 3.46.[11]

The two-dimensional integral over the crater surface is performed separately for ϕ and θ. For each, a Simpson quadrature algorithm has been implemented which adaptively refines the step width until the user-defined fractional accuracy goal is

[11] A class that integrates Lagerros' approximation eqn. 3.43 has also been implemented—it differs from that considered herein by a mere redefinition of a constant parameter.

reached (see, e.g., Press et al., 1992, chapt. 4).

Care was taken to minimize the number of calls to the numerically expensive trigonometric functions. E.g., in the polar integral the variable θ is transformed into $z = \cos\theta$ such that $\int_0^{\gamma/2} \sin\theta \mathrm{d}\theta$ becomes $-\int_{\cos\gamma/2}^1 \mathrm{d}z$.

With thermal inertia As has been discussed in sect. 3.2.3.f, thermal conduction inside craters is modeled in an approximative way. Model fluxes are calculated by objects belonging to the class `InertiaTimesCraterLagerros`, which own respectively one instance of `HemisphericNoInertia` and of `ThermalInertiaOnlyConvex`.

The `ThermalInertiaOnlyConvex` object is used to calculate the temperature at a smooth surface patch with thermal conduction. If the Sun is below local horizon ($\mu_S \leq 0$), the crater routine is not called, and fluxes are returned corresponding to that temperature. Otherwise, the ratio of the temperature with and without thermal conduction is determined (without thermal inertia, $T/T_{SS} = \sqrt[4]{\mu_S}$) and clipped to be ≤ 1.3 (see discussion in sect. 3.2.3.f). "Cratered" model fluxes are calculated with a rescaled temperature distribution. This is accomplished without changes to the implementation of `HemisphericNoInertia` by using a trick which is based on the fact that `fluxModFactors` is a function of λT, hence rescaling the temperature T is equivalent to rescaling the wavelength λ by the same factor (note that the coefficient of the Planck function containing λ^{-5} is not multiplied in `fluxModFactors` but in the calling function). Different fractional accuracy goals can be chosen for the `HemisphericNoInertia` and `ThermalInertiaOnlyConvex` objects.

3.4 Validation

In this section, tests for internal model consistency are reported, with an emphasis on validating the model for application to NEA data, i.e. for large phase angles ($> 30°$) and for thermal inertias up to 2500 J $\mathrm{s}^{-1/2}\mathrm{K}^{-1}\mathrm{m}^{-2}$. Another important model validation was its application to thermal-infrared observations of a well-studied reference NEA, (433) Eros, which will be reported in sect. 6.1.

3.4.1 Thermal conduction

A first qualitative validation of our thermal-conduction model is from visual inspection of Fig. 2.2 on p. 29, which was generated using the TPM code. As required, increasing thermal inertia reduces the diurnal temperature contrast and

shifts the temperature peak towards the afternoon side. Additionally, the peak temperature at low thermal inertia approaches the theoretical value of T_{SS} around 376 K (for the parameters specified), while for large thermal inertia the essentially constant temperature approaches $T_{SS}/\sqrt[4]{\pi}$ (see sect. 2.4.2) or roughly 283 K as required.

Due to conservation of energy, the thermally emitted power integrated over one asteroid revolution must match the total absorbed solar power. This was numerically checked, using the discretization parameters stated at the end of sect. 3.3.2, a fractional accuracy goal of 0.001, and assuming the situation depicted in Fig. 2.2—i.e., facet at the equator, $r = 1.1$ AU, $A = 0.1$, $\mathcal{P} = 6$ h. For a thermal inertia of 10,000 J $s^{-1/2}K^{-1}m^{-2}$, the total model emission was found to be too low by roughly 16 %, around 4 % too low for 2500 J $s^{-1/2}K^{-1}m^{-2}$, and around 1 % for 50 J $s^{-1/2}K^{-1}m^{-2}$. Tightening the fractional accuracy goal to 0.0001 incurs a penalty of largely increased program run time, but leads to a conservation of energy to within 1.5 % for thermal-inertia values up to 10,000 J $s^{-1/2}K^{-1}m^{-2}$, to 0.4 % for thermal inertia up to 2,500 J $s^{-1/2}K^{-1}m^{-2}$, and much better for lower thermal inertia. No asteroid studied to date displays a thermal inertia larger than 1000 J $s^{-1/2}K^{-1}m^{-2}$, hence a fractional accuracy goal of 0.001 is typically sufficient.

We wish to stress that the numerical effort for sufficiently accurate modeling of thermal conduction increases with thermal inertia; TPM codes suitable for MBAs may therefore be unsuitable for NEAs with typically much larger thermal inertia.

3.4.2 Beaming without thermal conduction

As detailed in sect. 2.2.3, thermal-infrared beaming is an enhancement relative to a Lambertian surface both in absolute flux level and in apparent color temperature for observations taken at low phase angles.

Figures 3.4, 3.5, and 3.6 show plots of crater fluxes relative to a flat Lambertian surface for hemispherical craters ($\gamma = 180°$) and for different viewing geometries (many other opening angles were tested, leading to qualitatively equivalent results). As expected, beaming not only enhances the flux at low phase angles (i.e. low zenith distances in Figures 3.4 and 3.5, low azimuthal distance in Fig. 3.6) but also the apparent color temperature: the flux ratio increases with decreasing wavelength. This is compensated for at large phase angles, when fluxes are reduced relative to a Lambertian emitter—more so at short wavelengths such that the color temperature is reduced relative to a Lambertian emitter.

An important consistency check is to verify the conservation of energy, i.e. to

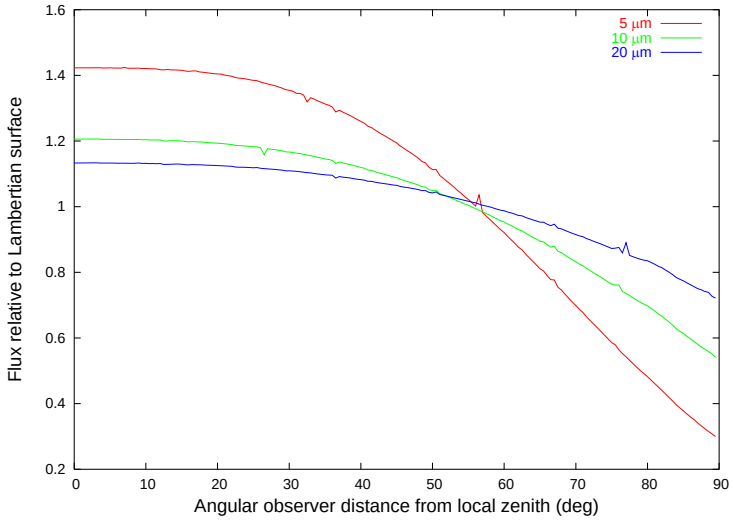

Figure 3.4: Relative flux enhancement due to a hemispheric crater ($\gamma = 180°$) as a function of observer angular distance from local zenith; the Sun is at local zenith. Further model parameters: $r = 1.1$ AU, $A = 0.1$, $\epsilon = 0.9$. The slight "wiggles" in the lines are due to numerical noise, they disappear for more stringent accuracy goals (we here use 0.001, a typical value).

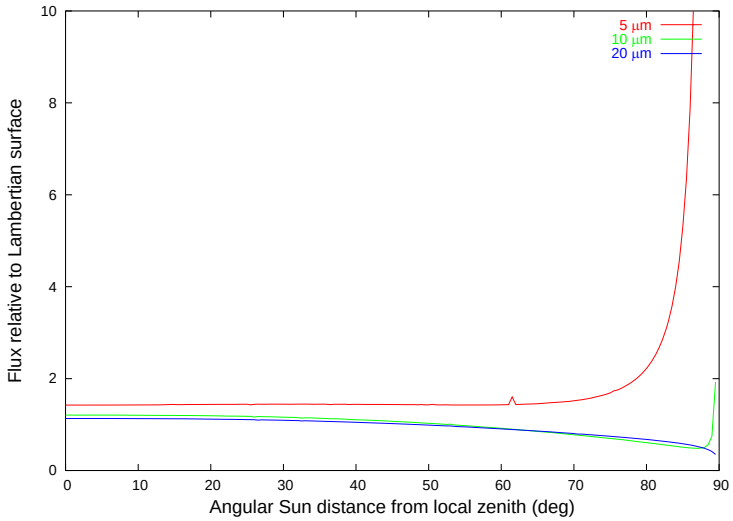

Figure 3.5: Relative flux enhancement as in Fig. 3.4, but as a function of solar angular distance from local zenith, with observer at local zenith.

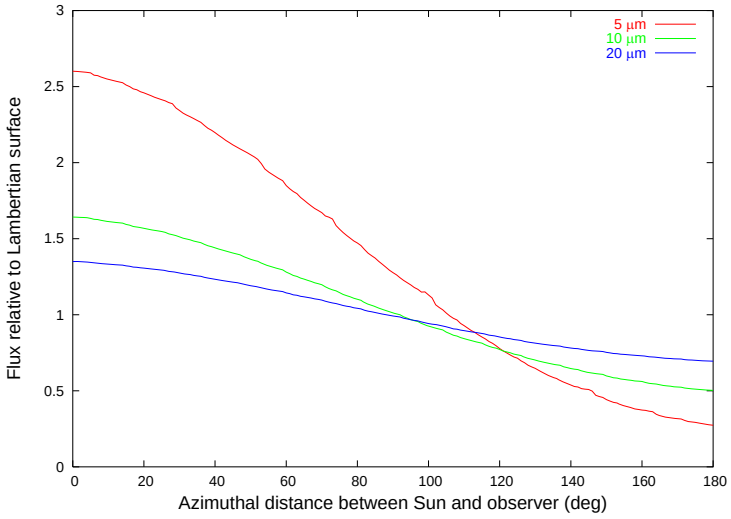

Figure 3.6: Relative flux enhancement as in Fig. 3.4 with both Sun and observer placed at a zenith distance of 45°, the azimuthal distance between the two is varied.

compare ingoing solar flux with the total outgoing energy. For a hemispherical crater of opening angle $\gamma = 180°$ and projected area of π this means

$$\pi \mu_S \left(1 - A_{\mathrm{corr}}\right) \frac{S}{r^2} = \int_0^\infty \mathrm{d}\lambda \int_{\mathcal{A}} \mathrm{d}\mathcal{A}\ F(\lambda) \tag{3.51}$$

for, e.g., a hemisphere $\mathcal{A}$ above the crater, with the observable flux eqn. 3.46 and the corrected Bond albedo eqn. 3.31.

Conservation of energy was tested by numerically integrating eqn. 3.51 for different values of solar zenith distance (assuming $r = 1.1$ AU, $A = 0.1$, and $\epsilon = 0.9$). To this end, the integral over $\mathrm{d}\lambda$ was discretized and truncated with 80 equidistant λ steps between 0.5 and 79.5 µm using the Simpson integration scheme (see, e.g., Press et al., 1992); for the integral over $\mathrm{d}\mathcal{A}$, a Monte-Carlo scheme was implemented with 2,500 uniformly distributed random directions towards the observer,[12] each Monte-Carlo integration was executed four times with identical parameters in order to gage the statistical noise. The typical scatter among the four runs is 1 %. In order to gage the absolute accuracy, disk-integrated thermal

[12] Note that the distribution of vectors resulting from uniformly distributed polar coordinates would *not* be uniform but rather biased towards the poles. Instead, we have drawn three Cartesian coordinates per vector uniformly distributed between −1 and 1 (0 and 1 for the z coordinate, so vectors are above local horizon) and rescaled the resulting vectors to unit length.

fluxes were generated for a spherical Lambertian emitter without thermal inertia and integrated those fluxes over $\mathrm{d}\lambda$ and $\mathrm{d}\mathcal{A}$. The resulting total thermal power emitted by the asteroid equals the total absorbed power to within the numerical noise (~ 1 %).

To check the crater routine for conservation of energy, it turned out to be convenient to check it against a Lambertian emitter. To this end, two integrals are calculated using the discretization above, where once the integrand is the output of the crater routine and once that of the Lambertian routine,[13] then the two resulting integrals are compared. Note that the crater induces a reduced albedo A_{corr} relative to the smooth surface (see sect. 3.2.3.c) due to the increased optical absorption inside the crater. Hence, the "crater integral" should be larger than the Lambertian integral by a factor of $(1 - A_{\mathrm{corr}})/(1 - A)$, which equals roughly 1.05 for the parameters considered here (see Fig. 3.2 on p. 67). For a fractional accuracy goal of 0.01, energy was seen to be conserved within 1 % (the Sun was placed at zenith distances of 0, 30, and 60°).

3.4.3 Beaming with thermal conduction

When thermal inertia is considered, ingoing and outgoing radiation are no longer in instantaneous equilibrium but only after integration over a asteroid revolution. The latter integral reduces to a mere sum of contributions from each of the `nTime` time steps, where for each the integral over $\mathrm{d}\lambda$ and $\mathrm{d}\mathcal{A}$ is performed as above. As in the case without thermal inertia, the integral over fluxes returned by an `InertiaTimesCraterLagerros` object are compared to the integral over Lambertian fluxes multiplied by $(1 - A_{\mathrm{corr}})/(1 - A)$.

Integration runs were performed for $\mathcal{P} = 6$ h, and the remaining parameters as in the rest of this section. The Sun was placed at an angular distance of 90° from the spin pole (i.e. over the equator), facets pointing 30, 60, and 90° away from the pole were considered, for thermal-inertia values of 50, 500, and 2500 J $\mathrm{s}^{-1/2}\mathrm{K}^{-1}\mathrm{m}^{-2}$. For a fractional accuracy goal of 0.0001 for the treatment of thermal inertia (as in the case of thermal inertia alone) and of 0.01 for cratering (as for cratering alone), energy was found to be conserved to within a few percent in all cases.

[13] In both instances, the `fluxModFactors` routines of the respective objects are called, hence returned values must be multiplied by λ^{-5}.

3.5 TPM fits to asteroid data

In principle, our TPM contains four parameters which can be varied independently to obtain the best fit to the data: the diameter D (which is related to p_V through the optical magnitude H), the thermal inertia Γ, the crater opening angle γ, and the crater density ρ_c. It has been shown by Emery et al. (1998) and Lagerros (1998a) that the modeled effect of surface roughness is practically a function of a single parameter, the mean surface slope $\bar{\Theta}$, which is a function of crater opening angle and crater density, reducing the dimensionality of the parameter space by one.

Originally (see Mueller et al., 2004), our approach was to fix the crater opening angle at a constant value and to determine the combination of diameter, thermal inertia, and crater density that best fit the data. In this approach we exploited the fact that, as discussed in sect. 3.1.2, model fluxes depend linearly on the assumed crater density. For a given combination of diameter and thermal inertia it is therefore possible to analytically determine the best-fit crater density through linear regression (with the constraint that the density must be non-negative and ≤ 100 %).

Later, however, we found that the crater roughness is often not significantly constrained by the data. We find it more instructive and more transparent to use four preset combinations of roughness parameters which span the range of possible surface roughness, and to determine the best-fit diameter and thermal inertia for each. The results are then compared with one another, potentially showing that some roughness model fits the data significantly better than others, and otherwise illustrating the range of roughness-induced uncertainty in thermal inertia and diameter. The four roughness models considered throughout this thesis are

No roughness $\gamma = 0$, $\rho_c = 0$

Low roughness $\gamma = 117.70116°$, $\rho_c = 0.4$

Default roughness $\gamma = 144.59046°$, $\rho_c = 0.6$

High roughness $\gamma = 151.75834°$, $\rho_c = 1.0$

The parameters for “low”, “default”, and “high” roughness have been defined by Müller et al. (2004, see also references therein) on the basis of thermal-infrared analyses of MBAs.

Synthetic thermal fluxes are generated for the observing geometry and at the wavelengths of the observational data. To fit diameter and thermal inertia for a given set of roughness parameters, model fluxes are calculated on an equidistant grid of thermal-inertia values from the largest value considered down to 0. For each value of thermal inertia, a best-fit diameter is determined from the assumed input diameter and the scale factor κ which minimizes

$$\chi^2 = \sum_{i=1}^{n} \left(\frac{\kappa \cdot m_i - d_i}{\sigma_i} \right)^2 \tag{3.52}$$

(for data points d_i with uncertainties σ_i and synthetic model fluxes m_i; see eqn. 2.17). The best-fit diameter and the corresponding χ^2 are stored. We neglect that changing the diameter is, for constant H, equivalent to changing the albedo, which in principle changes model temperatures and thermal fluxes in a nontrivial way. A full recomputation of model fluxes would, however, be computationally very expensive. We would expect that it is safe to neglect the influence of albedo on temperature if p_{V} is reasonably constant, i.e. if the resulting κ value is close to unity (see also sect. 2.5.4).

For the first (largest) thermal-inertia value considered in each series, an arbitrary default-value of p_{V} is used. For all following steps, model fluxes are calculated assuming the best-fit p_{V} determined in the previous thermal-inertia step. For not too large steps in thermal inertia, κ typically stabilizes to values close to unity within a small number of iterations (see, e.g., sect. 6.1.3 for a discussion) such that our approximation above becomes uncritical.

For each roughness model, an ASCII file is output which can be used as a data file for GNUplot. Those files contain, among other things, data lines with entries for thermal inertia, the best-fit χ^2 obtained, and the corresponding best-fit p_{V}. Best-fit roughness models, thermal inertias, and diameters are then determined from an analysis of the obtained plots (see, e.g., sect. 6.1.3). The run time scales with the number of data points and the number of facets in the shape model, typical values range between a few hours and a few days on a 2.66 GHz PC.